Research Article

High repetition rate ultrafast laser-structured nickel electrocatalyst for efficient hydrogen evolution reaction

Zaiwei Cai [a,†] **Zihao Li,** [a,†] **Yingtao Zhang,** [a] **Chiyi Wei,** [a] **Hao Tian,** [a] **Molei Hao,** [a] **Xiaoming Wei** [a,b,c,d,*] **and Zhongmin Yang** [a,b,c,d,e,*]

[a]South China University of Technology, School of Physics and Optoelectronics, Guangzhou, China
[b]South China University of Technology, State Key Laboratory of Luminescent Materials, Guangzhou, China
[c]South China University of Technology, Guangdong Engineering Technology Research and Development Center of Special Optical Fiber Materials and Devices, Guangzhou, China
[d]South China University of Technology, Guangdong Provincial Key Laboratory of Fiber Laser Materials and Applied Techniques, Guangzhou, China
[e]South China Normal University, Research Institute of Future Technology, Guangzhou, China

Abstract. Laser processing with high-power ultrashort pulses, which promises high precision and efficiency, is an emerging new tool for material structuring. High repetition rate ultrafast laser highlighting with a higher degree of freedom in its burst mode is believed to be able to create micro/nanostructures with even more variety, which is promising for electrochemical applications. We employ a homemade high repetition rate ultrafast fiber laser for structuring metal nickel (Ni) and thus preparing electrocatalysts for hydrogen evolution reaction (HER) for the first time, we believe. Different processing parameters are designed to create three groups of samples with different micro/nanostructures. The various micro/nanostructures not only increase the surface area of the Ni electrode but also regulate local electric field and help discharge hydrogen bubbles, which offer more favorable conditions for HER. All groups of the laser-structured Ni exhibit enhanced electrocatalytic activity for HER in the alkaline solution. Electrochemical measurements demonstrate that the overpotential at 10 mA cm^{-2} can be decreased as much as 182 mV compared with the overpotential of the untreated Ni (-457 mV versus RHE).

1 Introduction

Due to the growth of the global population and the development of society, the consumption of exhaustible fossil fuels is increasing, which leads to environmental deterioration, global warming, and the energy crisis.[1] Therefore, there is an urgent need to find a replacement for nonrenewable energy sources. Hydrogen is an attractive energy carrier due to its high-energy density, clean property, and high availability.[2,3]

As a sustainable hydrogen production strategy, electrolysis of water has achieved large-scale and mature commercial hydrogen production.[3] However, due to the high cost of the efficient noble metal hydrogen evolution reaction (HER) electrocatalysts, such as platinum (Pt),[4] ruthenium (Ru),[5] and iridium (Ir),[6] searching for non-noble metal-based electrocatalysts is significantly important.[7] As one of the most promising candidates for non-noble metal electrocatalyst, nickel (Ni) possesses the lowest hydrogen adsorption free energy and the highest HER exchange current density among non-noble metals in alkaline solution[8] and has the advantages of high conductivity, high oxidation resistance, as well as abundant reserve,[1] and thus draws great interest.

---

*Address all correspondence to Xiaoming Wei, xmwei@scut.edu.cn; Zhongmin Yang, yangzm@scut.edu.cn

†These authors equally contributed to this work.

Enlarging the surface area and subsequently increasing the number of electrochemically active sites on the electrocatalyst is an important strategy for improving the performance of the electrocatalyst.[9] Common methods to increase the surface area of electrocatalysts include chemical coating,[10] electrodeposition,[11] electrospraying,[12] a combination of mechanical alloying and chemical leaching,[13] and template methods.[14,15] However, micro/nanomaterials prepared by chemical coating and electrospraying possess low structural stability, template method produces polluting byproducts, and electrodeposition only generates irregular structures,[1] while the combination of mechanical alloying and chemical leaching is relatively time- and cost-consuming. An ultrafast laser, with its ultrashort pulse width and high peak power, enables extreme processing conditions,[16] making it a novel way to modify the optical,[17–19] electrical,[20,21] mechanical,[22] and chemical[23,24] properties of materials through introducing micro/nanostructures onto the surface of the material,[25–27] and the micro/nanostructures can be flexibly adjusted by tuning the laser parameters.[28,29] Ultrafast laser structuring has the advantages of high efficiency, high controllability, high precision, being environmental friendly, and producing stable micro/nanostructures,[30] and therefore, it is also considered an important method to be applied in electrocatalyst fabrication.[31] The micro/nanostructures brought by ultrafast lasers increase the surface area of the electrocatalysts and add reaction sites.[30] The accumulation of free electrons on the tip of the micro/nanostructures generates a strong local electric field,[31] which can be conducive to water dissociation, adsorption of H^+, and the combination of the adsorbed hydrogen atoms, and therefore enhances HER kinetic activity. In addition, ultrafast laser structuring also alters the surface wetting behavior of materials,[32,33] which favors the infiltration of electrolyte and reduces the impedance of the electrode/electrolyte interface.[34,35] Gabler et al.[36] used the ultrashort pulse laser to form laser-induced periodic surface structure (LIPSS) on Ni and reduced the overpotential by 23 and 165 mV at $-0.3 \, A \, cm^{-2}$ before and after cyclic voltammetry (CV) activation, respectively, in comparison to smooth Ni. Rauscher et al. also demonstrated that through tweaking the laser structuring parameters the surface roughness of Ni can be tuned to generate different microstructures. The lowest overpotential of 280 mV at $-0.3 \, A \, cm^{-2}$ was obtained by the femtosecond-laser structured Ni electrode with conical microstructures, which is a reduction of ~45% compared with smooth Ni.[37] Neale et al.[38] used two laser systems with repetition rates ranging from 1 to 50 kHz to form LIPSS with a period approximately equal to the wavelengths of the lasers on Ni, and the formation of the LIPSS increased the electrochemical activity of the structured Ni relative to unstructured Ni by 2.5 times. Poimenidis et al.[1] used a laser with a repetition rate of 1 kHz and a wavelength of 795 nm to form LIPSS with the average period of 570 nm and decorated with nanometer-sized features, which resulted in 3.7 times higher hydrogen production efficiency compared with unstructured Ni.

The high repetition rate laser with intrapulse repetition rate in the order of gigahertz is a novel tool for laser structuring, which can reduce the minimum average power required to reach the ablation threshold of a material.[39] When the repetition rate of a pulsed laser is high enough, heat accumulation occurs between two neighboring pulses within the irradiated area, which is an effect absent in low repetition rate laser processing. When a high repetition rate laser operates in the burst mode through modulation, its burst envelope, burst duty ratio, and interburst repetition rate are all adjustable. Therefore, the high repetition rate ultrafast laser possesses even more degrees of freedom and thus can endow the substrate with an even greater diversity of micro/nanostructures. This is an incomparable advantage over pulsed lasers with low repetition rate. Here we report for the first time, we believe, using a homemade modulable high repetition rate ultrafast laser working under different conditions to generate different micro/nanostructures on Ni electrodes. The surface morphology and the electrochemical properties of the untreated and laser-structured electrodes are studied. Our results show that by tuning the parameters of laser structuring, self-organized worm-shaped microstructures and parallel grooves can be formed under low scan speed, high scan number, and high-pulse fluence, respectively. Compared with bare Ni electrodes, the electrocatalytic performances of the laser-structured Ni electrodes are all significantly improved.

2 Results and Discussion

2.1 Laser Structuring Parameters

To take full advantage of the multi-degree-of-freedom characteristics of the modulable high repetition rate laser, three groups of drastically different laser structuring conditions were applied to fabricate three groups of samples, denoted as low scan speed group (S), high scan number group (N), and high-pulse fluence group (F). Among them, the low scan speed group has the highest deposited energy per unit area because of the smallest scan pitch distance and the lowest scan speed. Combined with the lowest incident laser power, the transversal mass transfer on these samples is promoted. The samples in this group are labeled S-2, S-4, and S-6 according to their scan numbers. The scan numbers of the high scan number group are 2 orders of magnitude higher than the other groups, which is beneficial for the longitudinal-wise development of the microstructures. The samples are labeled N-50, N-150, and N-250, according to the scan speeds of the laser during structuring. The high-pulse fluence group was structured with the highest incident laser power as well as the highest pulse fluence, and therefore theoretically the highest ablation rate. The samples are labeled F-1, F-2, and F-3 according to their scan numbers. Among the three experimental laser parameters, the low scan speed group was structured by the lowest average laser power, which corresponds to a fluence right above ablation threshold. Therefore, the ablation threshold of Ni in this experiment can be calculated to be $3.3 \, mJ \, cm^{-2}$. However, the single-pulse ablation threshold of Ni reported by Torrisi et al.[40] is $900 \, mJ \, cm^{-2}$ using laser with 1064 nm wavelength, 3 ns pulse width, and 10 Hz repetition rate. The reduction of ablation threshold in our experiment is believed to be from the result of the heat accumulation effect of high repetition rate pulsed laser.

2.2 Surface Morphology and Composition

Scanning electron microscopy (SEM) was applied to study the surface morphology of different samples. As shown in Figs. 1(a)–1(c), all samples in the low scan speed group consisted of self-organized worm-shaped microstructures with redeposited nanoparticle aggregates on top;[41] a zoom-in view of hierarchical micro/nanostructure is shown in the inset of Fig. 1(c). The highest deposited energy per unit area and the lowest incident laser power lead to the large heat dissipation distance and long heat relaxation time, which allow continuous

material heating without ablation and in-plane material transfer resulting from the competing destabilization and dissipation forces that occur in the transiently laser-induced molten surface:[42] First, laser induces the formation of randomly distributed humps on the Ni surface, and then the humps gradually extend and merge with neighboring humps and form the worm-shaped microstructures, which are eventually covered by the molten redeposited nanoparticles.[43] This self-organizing process is also indicated by the fact that the worm-shaped microstructures grew almost irrespective of the scan direction of the laser and evenly spread through the whole surface of irradiated Ni. It can be deduced that once the self-organized microstructures are induced the laser scan number has little influence on their development. However, the nanoparticle aggregates accumulate with the increase of the scan number. The hierarchical micro/nanostructures increase the surface area, while the nanoparticle aggregates are also masking the grooves when their density becomes high enough, which might cover up the active surface area in the grooves.

Distinguishing differences can be found in the high scan number group as shown in Figs. 1(d)–1(f). Because of the high scan number, materials within the scan track are repeatedly removed, leaving parallel straight grooves on the surface of Ni. Between the grooves are ridges where Ni was not irradiated by laser. By increasing the scan speed from 50 to 250 mm s⁻¹, the integrity of the ridges decreases with the increase of scan speed due to the more abrupt change in temperature during the faster scanning, introducing a large number of nanoparticles, as shown in the inset of Fig. 1(f).

Intuitively, high-pulse fluence group samples structured with the highest pulse fluence should have the deepest grooves. However, as shown in Figs. 1(g)–1(i), the resulting grooves of high-pulse fluence group samples are shallower than those of the high scan number group samples. Because of the highest incident laser power, yet much slower scan speed of the high-pulse fluence group as compared with the high scan number group is believed to spawn a stronger shield effect. Therefore, the ablation rate in this group is lower, as indicated by the relatively flat surface of the samples and the increase in scan number-only results in the notable enlargement of the width (but not the depth) of the grooves because of the widened heat affected zone. Few nanoparticles can be found on the samples in this group. It is speculated that the plasma and particles that contributed to the shielding effect are soon pushed back to the surface when they are still in liquid phase rather than partially solidified as in the low scan speed group and thus do not favor nanoparticle formation.

The micro/nanostructures on the first two groups of samples are introduced via distinct mechanisms. On the low scan speed group samples, laser irradiation induces the random formation of the humps, and the humps merge to form worm-shaped microstructures, which are later nonselectively covered by molten redeposition nanoparticles, as illustrated in Fig. 2(a). In contrast, the grooves on the high scan number group samples are structured by direct laser writing, and the nanoparticles are generated through fragmentation of the ridges, and thus their existence is limited within the areas with no laser irradiation, as illustrated in Fig. 2(b).
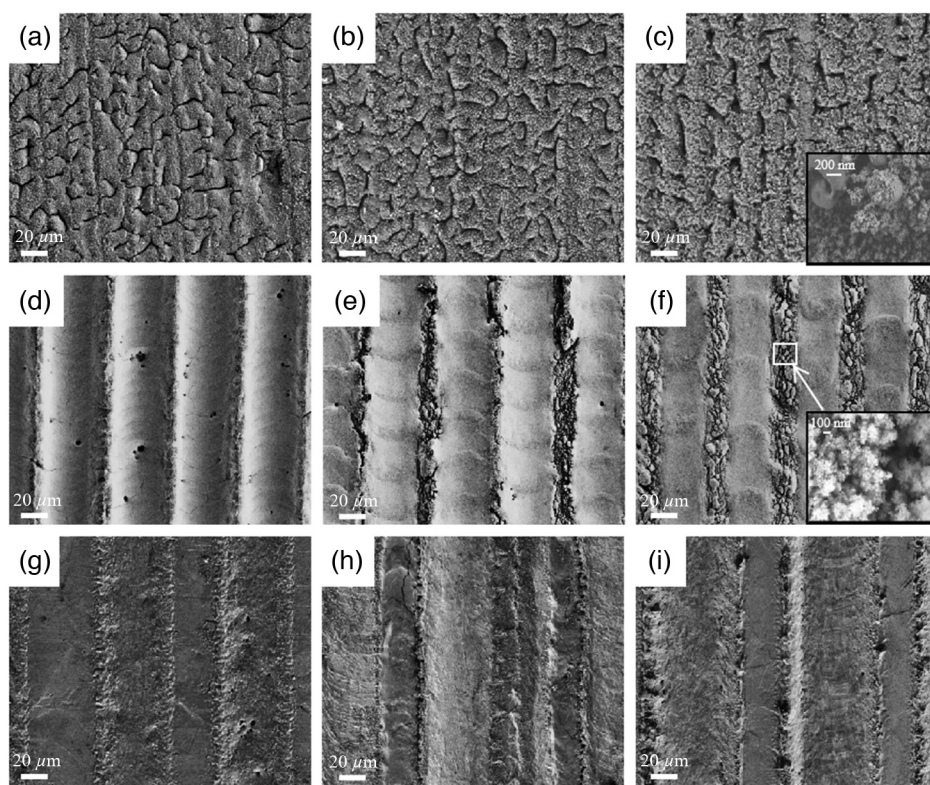
Fig. 1 SEM images of (a)–(c) low scan speed group samples S-2, S-4, and S-6; (d)–(f) high scan number group samples N-50, N-150, and N-250; and (g)–(i) high-pulse fluence group samples F-1, F-2, and F-3.
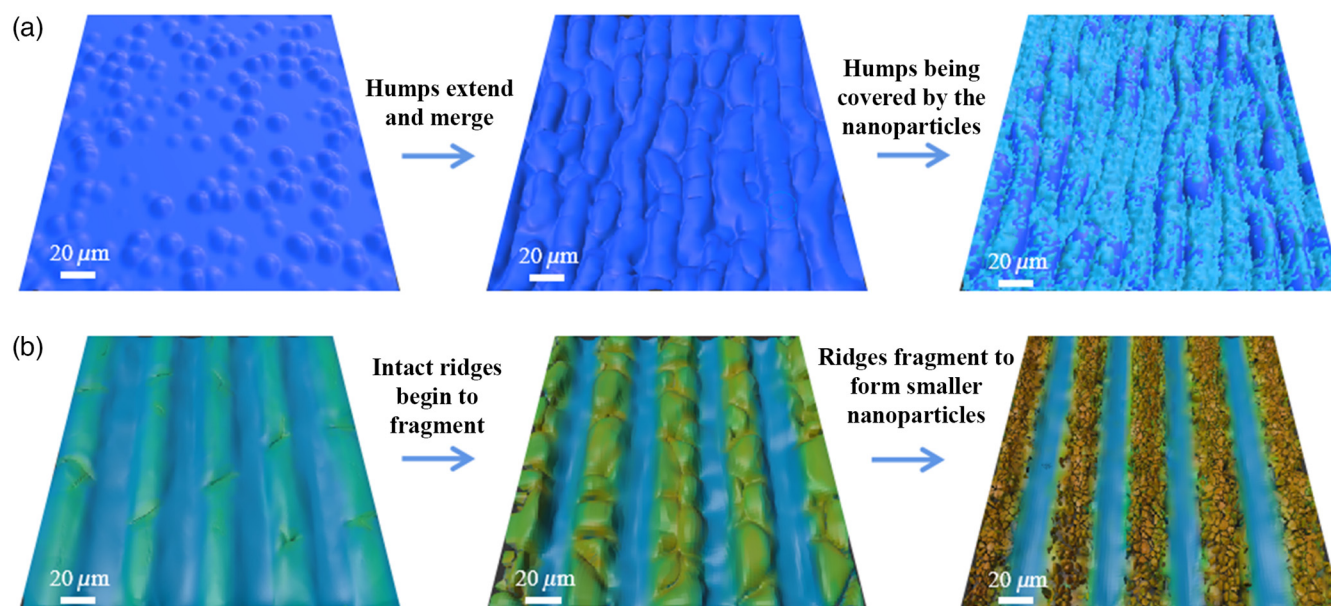
Fig. 2 Schematic illustration of the morphology formation processes of (a) a low scan speed group sample and (b) a high scan number group sample.
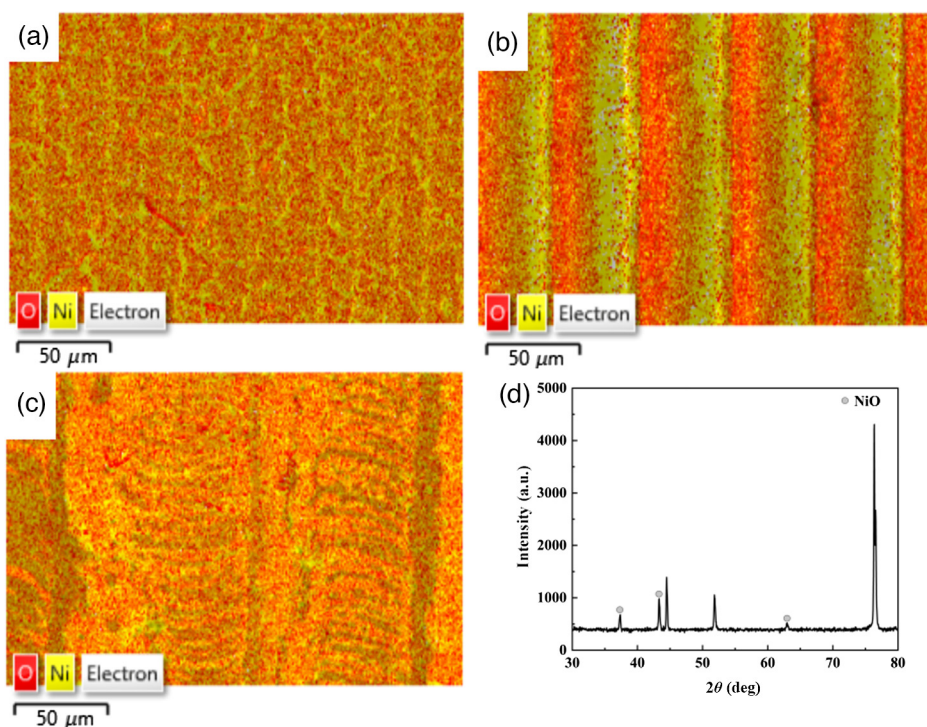
Fig. 3 Energy-dispersive spectroscopy mapping images of (a) S-2, (b) N-150, and (c) F-3. (d) XRD pattern of S-2.

As shown in Fig. 3, energy dispersive spectroscopy was executed to characterize elemental composition and distribution of sample S-2 of the low scan speed group, sample N-150 of the high scan number group, and sample F-3 of the high-pulse fluence group. It can be observed that all of the samples contained oxygen on their surfaces. Oxygen atoms on S-2 and F-3 distribute almost uniformly on the entire Ni surface, whereas the oxygen atoms on N-150 were mainly distributed on the ridges. The x-ray diffraction (XRD) pattern of sample S-2 is represented in Fig. 3(d). Three diffraction peaks at 37.3, 43.3, and 62.9 deg can be indexed as the cubic crystal system of NiO, which further confirms the existence of NiO.

2.3 Electrochemical Performance

For the HER process in alkaline solution, electrolysis of water involves two main steps. The first step is the Volmer process [Eq. (1)], which is the combination of protons and electrons in the solution to form adsorbed hydrogen atoms (H*) on the electrode surface (M). The second step can be divided into two possible reactions. The first possible reaction is that another water molecule donates a proton to the adsorbed hydrogen atom, and they combine with a second electron to produce H_2 [Heyrovsky process, Eq. (2)]. The second possible reaction is that the second H* generated by repeating the Volmer process combines with the first H* Tafel process [Eq. (3)]:[8]

$$H_2O + M + e^- \rightleftharpoons M - H* + OH^-, \qquad (1)$$

$$H_2O + e^- + M - H* \rightleftharpoons H_2 + OH^- + M, \qquad (2)$$

$$2M - H* \rightleftharpoons H_2 + 2M. \qquad (3)$$

Therefore, being conducive to the formation of protons and adsorption of hydrogen atoms is the key to better electrocatalytic activity. Laser structuring of Ni samples can promote these processes.

Figure 4 shows the linear sweep voltammograms of a bare Ni electrode and the three groups of laser-structured Ni electrodes. Linear sweep voltammetry (LSV) reveals the HER electrocatalytic ability of the Ni electrodes. When operating at the same current density, the electrode that requires lower applied voltage possesses higher electrocatalytic activity. It can be observed that the current density on the bare Ni electrode reached 10 mA cm^{-2} at -457 mV versus reversible hydrogen electrode (RHE), and all laser-structured Ni electrodes presented enhanced electrocatalytic activity compared with the bare Ni electrode.

In the low scan speed group, the current density of 10 mA cm^{-2} is reached at almost the same potential of -329 mV versus RHE for all three samples, as shown in Fig. 4(a). Although heat treatment or anodization is usually needed for the oxide layer formation of ultrafast laser-structured metal-based electrocatalyst, as the heat affected zone (HAZ) of ultrafast laser structuring is relatively small,[44] the slow scan speed we applied in the structuring of electrodes in this group enables a long-duration high-temperature environment that favors the oxidation of Ni. The electrocatalytic activity of the samples received promotion from

the synergistic effect of Ni/NiO—Ni and Ni^{2+} species enhances H and OH$^-$ adsorption, respectively, and thus facilitates the Volmer process.[45–47] As indicated by the SEM images, the extended surface area results from the laser-induced self-organized worm-shaped microstructures, along with the accumulation of nanoparticles brought by the increase in scan number, which also contributes to the increase of the activation sites. It is suggested that the tip of the nanoparticle aggregates can converge the local electric field and thus accelerate the charge transfer and benefits the Volmer and Heyrovsky processes of HER.[31] Nevertheless, as revealed by LSV, the Ni/NiO synergy and the surface area increment are likely canceled out by the masking of redeposition, which not only covers the ridges of the microstructures but also fills up the grooves. Therefore, the number of laser scans shows only a limited effect on the electrocatalytic activity of low scan speed group samples.

The high scan number group Ni electrodes significantly reduce the overpotential toward HER compared with the low scan speed group electrodes, as shown in Fig. 4(b), and it can also be found that the reduction in overpotential in this group also increases with the increase of the laser scan speed. N-50, N-150, and N-250 achieved 10 mA cm^{-2} at -313, -275, and -286 mV versus RHE, respectively. At a higher current density of -0.3 A cm^{-2}, the reduction of overpotential of N-250 exceeds that of N-150 by 16 mV. It is speculated that the high scan speed during the structuring process of the samples in this group allows the laser beam to elude the plasma and particle shielding, and thus enhances the ablation and introduces large numbers of nanoparticles, leading to improved electrocatalytic property toward HER. However, the elevation of electrocatalytic property from N-150 to N-250 is smaller than the promotion from N-50 to N-150, which can be attributed to the existence of a certain maximum speed that is required for the laser beam to fully get rid of the shielding effect; after reaching the critical value, further accelerating the scan speed will no longer be beneficial to the structuring. Additionally, the grooves introduced by laser structuring can be used to channel and discharge the H_2 bubbles generated in the HER process, preventing them from blocking the active area,[48] which also promotes the Heyrovsky and Tafel processes.

In the voltammogram of the high-pulse fluence group [Fig. 4(c)], it can also be found that the reduction in overpotential of the samples in this group also increases with the increase of the laser scan number. F-1, F-2, and F-3 achieved 10 mA cm^{-2} at -333, -306, and -289 mV versus RHE, respectively. It is speculated that the increase in scan number
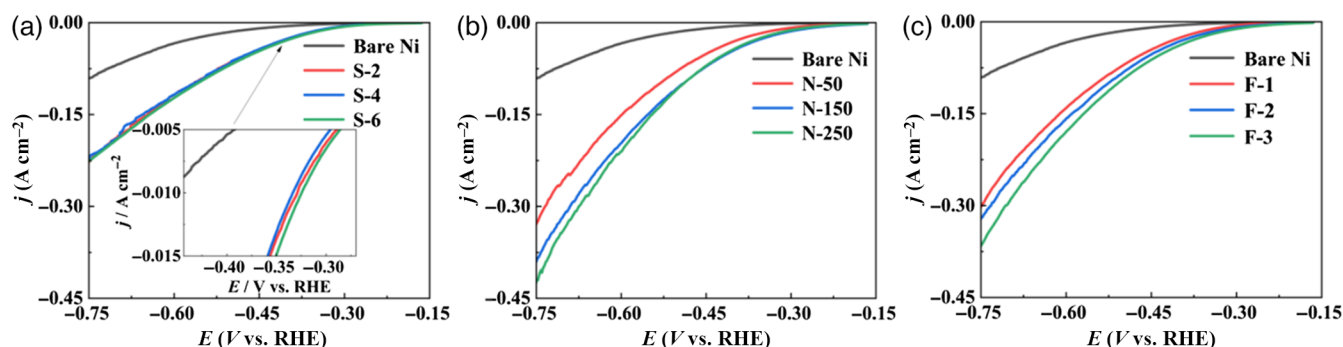
Fig. 4 Linear sweep voltammograms of (a) low scan speed group, (b) high scan number group, and (c) high-pulse fluence group and bare Ni electrodes.

deepens the grooves as well as roughens the surface and thus slightly increases the surface area and improves the HER electrocatalytic performance. However, the high-pulse fluence group electrodes are still inferior to the high scan number group, as the ablation is far less significant.

Figure 5 presents the electrochemical impedance spectra of bare Ni and the three groups of laser-structured Ni electrodes at open circuit potential in 1 mol L^{-1} KOH solution. All the recorded electrochemical impedance spectra (EIS) are fitted using the same equivalent circuit, shown in Fig. 5(d). Since the Nyquist plots do not contain perfect semicircles, the capacitors in the Randles model are replaced by constant phase elements (CPEs) to compensate for the frequency dispersion resulting from surface inhomogeneity.[49] The equivalent circuit is composed of the solution resistance R_s and three pairs of resistance and corresponding CPE ($R//CPE$) in series.[7,36] The first, second, and third semicircles counting from high- to low-frequency region correspond to the impedance of solid-electrolyte interface ($R_{SEI}//Q_{SEI}$), solid-state diffusion ($R_{sd}//Q_{sd}$), and charge transfer ($R_{ct}//Q_{ct}$), respectively. The smaller the semicircles are, the lower the corresponding impedances will be. It can be observed that the impedances of the laser-structured electrodes are all smaller than that of the bare Ni electrode.

As revealed by the fitting, in the low scan speed group, all the resistances except R_s experience an increase followed by a decrease when the scan number grows from 2 to 6, which can be attributed to the induction of the self-organized microstructures, the masking of microstructures by the nanoparticles, and the formation of the hierarchical micro/nanostructures. The dual-scale structures not only enhance the local electrical field but also provide a porous interface that is more beneficial to electrolyte penetration and gas transport.[7] A similar effect can also be observed in the high scan number group, and R_{ct} drop can be found when

the laser scan speed reaches 150 mm s^{-1}, since nanoparticle generation is induced. R_{sd} also decreases from 76 Ω cm^2 of N-50 to below 20 Ω cm^2 because of the thinner oxide layer resulting from the weaker shielding effect and therefore stronger ablation.

As for the high-pulse fluence group, all the resistances except R_s follow the tendency to decline. R_{SEI} and R_{sd} gain a particularly large reduction when increasing the scan number from 2 to 3, which might be indicating the formation of a loose oxide layer, and it is speculated that the first two scans contributed to the accumulation of heat that yields the oxide layer.

Observing electrode potential at a constant cathodic current for a given time is a simple way to study the stability of the electrocatalytic performance of a given electrocatalyst. It can be observed that, other than unstructured Ni, most electrodes reached a relatively stable state after 1 h of chronopotentiometry (CP). This result indicates the superior electrocatalytic stability of the laser-structured Ni electrodes, which is important for the practical application of large-scale electrocatalytic hydrogen production with Ni electrodes.

It can be seen from Fig. 6(a) that S-2 without the masking of nanoparticles has the poorest HER stability compared with other electrodes in this group.[50] It is suggested that the exposed oxide layer cannot long withstand the reducing environment during HER, and therefore gradually loses the feature of Ni/NiO synergy. For comparison, both S-4 and S-6 have a large number of redeposited Ni nanoparticles covering the oxide layer on the self-organized worm-shaped microstructures and protect their oxide layer from reduction. It is speculated that the nanoparticles are molten when being ejected and redeposited, and thus they are tightly attached to the oxidized surface and will not easily fall off, leading to the better stability of S-4 and S-6.
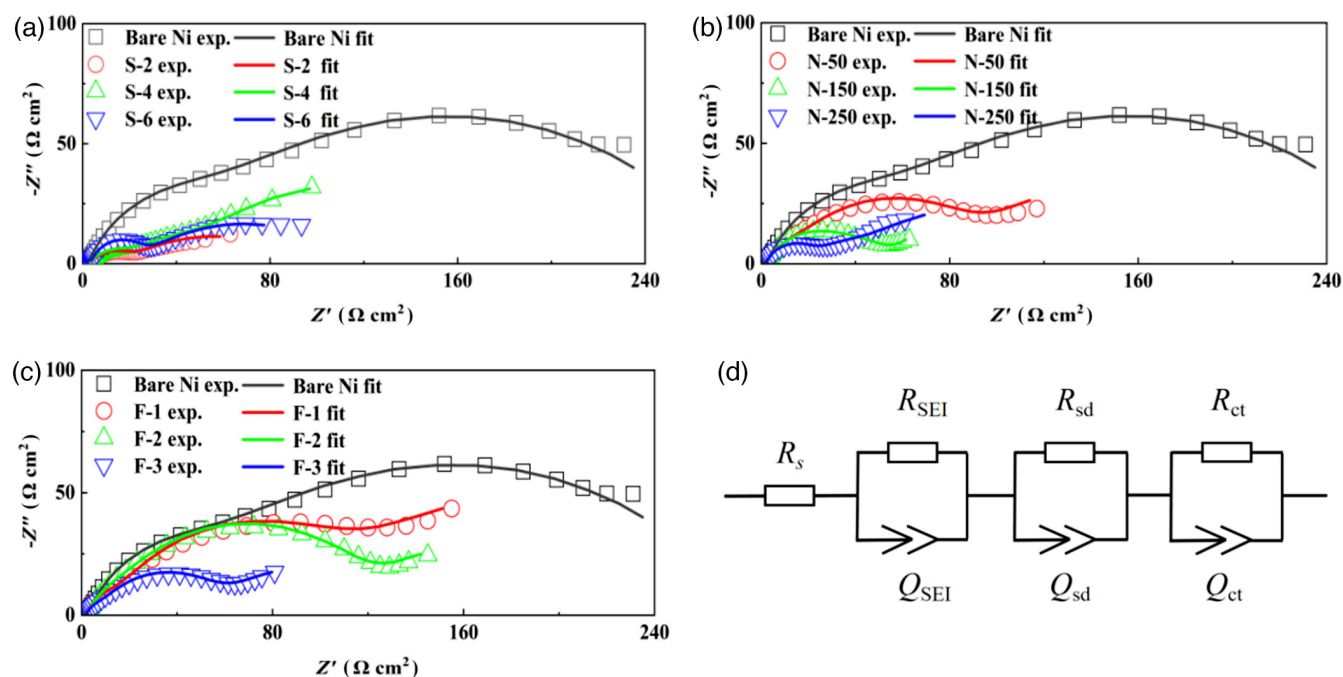
Fig. 5 Electrochemical impedance spectra and the corresponding fitted curves of (a) low scan speed group, (b) high scan number group, and (c) high-pulse fluence group and bare Ni electrodes. (d) Equivalent circuit used for fitting.
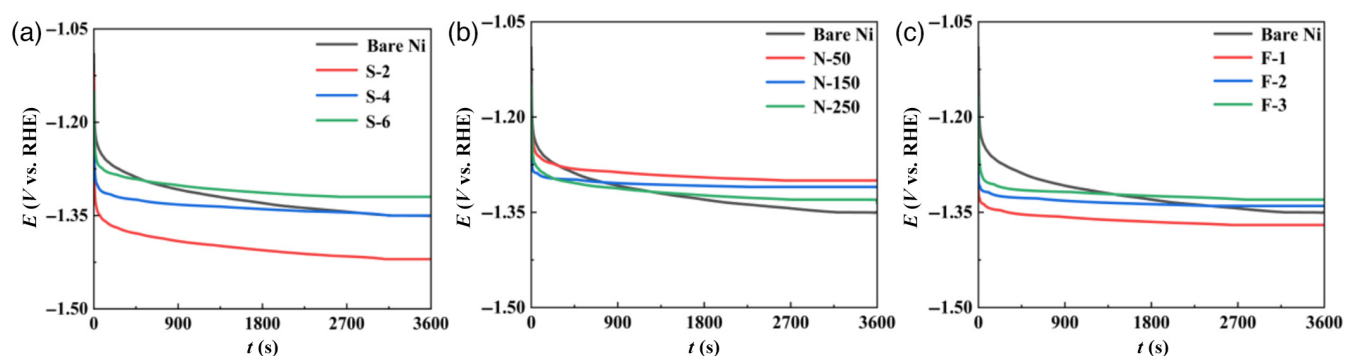
Fig. 6 Chronopotentiograms of (a) low scan speed group, (b) high scan number group, and (c) high-pulse fluence group and bare Ni electrodes.

The order of the stability in the high scan number group is exactly in the opposite order of the electrocatalytic activity, as shown in Fig. 6(b). N-50 is the most stable in this group, whereas N-250, with the best electrocatalytic performance, exhibits the worst stability. N-50 presented the lowest overpotential toward HER among all electrodes after the 1-h CP measurement. This trend can be attributed to the possibility that the nanoparticles in N-150 and N-250 are relatively loose and can easily fall off, since they are formed by the fragmentation of the metal caused by rapid expansion and contraction during laser scanning[51] compared with the redeposited nanoparticles of the low scan speed group electrodes.

The three electrodes of the high-pulse fluence group display similar stability [Fig. 6(c)]. Since only simple microstructures are introduced by laser structuring, the structural stability of the electrodes in this group is generally higher.

3 Conclusion

In this study, we used a homemade high repetition rate ultrafast fiber laser working under various conditions to structure Ni plates, which introduces different micro/nanostructures and alters the surface composition of the material. The results show that it can facilitate the close wetting of the electrode by the electrolyte, reduce the contact resistance of the interface, accelerate the transfer of charge, and improve the efficiency of the electrocatalysis. The electrocatalytic activity and the stability of all laser-structured Ni electrodes were investigated by LSV. It can be observed that the overpotential of the three groups of laser-structured Ni electrodes are all reduced compared with bare Ni. EIS studies indicate the controllable formation of micro/nanostructures and oxidation layers under different conditions. The stability of the laser-structured electrodes is also improved, as revealed by CP. In the low scan speed group, the increase of surface area resulting from laser-induced self-organized microstructures and the accumulation of nanoparticles. It is also suggested that the nanoparticle aggregates can converge the local electric field and thus accelerate the charge transfer. The high scan number group Ni electrodes significantly reduced the overpotential toward HER compared with the low scan speed group electrodes. Due to the more abrupt change in temperature during the faster scanning, the ridges fragment into nanoparticles and thus improve the electrocatalytic performance. It is also suggested that simply raising the power of the laser might not result in a better electrocatalytic

performance of the electrode because of the accompanied heavier shielding effect.

4 Experimental Section

High-purity Ni sheet (99%, Shanghai Yexin Nonferrous Metals Co., Ltd.) with a thickness of 0.3 mm was cut into square pieces. A homemade high repetition rate ultrafast fiber laser was used to generate laser with pulse width of 25 ps and pulse repetition rate of 1.2 GHz at the center wavelength of 1064 nm. The beam quality M^2 of the output laser beam is measured to be 1.10 and 1.02 for the x and y directions, respectively. The laser pulses were modulated using an acousto-optic modulator so that the laser can operate in the burst mode with a modulation frequency from 1 kHz to 1 MHz. The laser was focused into a tight spot with a radius of 20 μm using a 100 mm-focal length field lens, and a galvo scanner was used to snake-scan the laser spot over the whole sample surfaces at different scan speeds, with the laser beam being kept perpendicular to the sample surfaces. The scanned area is a square with 5 mm side length. The laser structuring process was carried out in the ambient atmosphere. Detailed laser processing parameters of the three groups of samples are shown in Table 1.

SEM (GemniSEM 500, Carl Zeiss AG) was used to take images of the surface of the laser-structured Ni samples at different magnifications. Energy dispersive spectroscopy (X-Max 80, Oxford Instrument) and XRD (X'Pert PRO, Malvern PANalytical) were used to characterize the surface composition of the laser-structured Ni samples. Before electrochemical measurements, the back sides of bare and laser-structured Ni samples were connected to copper wires through soldering and then sealed with waterproof adhesive. The electrochemical measurements were performed in a three-electrode electrolytic cell with bare or laser-structured Ni as the working electrode, Pt as the counter electrode, and Ag/AgCl in 3.5 mol L^{-1} KCl solution as the reference electrode. 1 mol L^{-1} KOH solution was used as an electrolyte. All the electrochemical measurements were performed using a CHI660E electrochemical workstation (Shanghai Chenhua Inc.). The scan rate of LSV was 5 mV s^{-1}, with a potential range from −0.764 to −0.164 V versus RHE. EIS measurements were performed at open circuit potential with 5 mV alternating current (AC) signal in the frequency range from 100 kHz to 10 mHz. Equivalent circuit of the EIS results was simulated using software Zview (Scribner Associates Inc.). The constant current applied in the CP measurements was −2.5 mA. All electrodes were activated using CV for five cycles

Table 1 Key parameters used in laser structuring of different groups of samples.

	Sample denotation	Scan speed (mm s^{-1})	Duty cycle (%)	Laser power (W)	Scan number	Scan pitch distance (μm)
Low scan speed group	S-2	0.75	20	9	2	20
	S-4				4	
	S-6				6	
High scan number group	N-50	50	50	12	200	50
	N-150	150				
	N-250	250				
High-pulse fluence group	F-1	5	5	40	1	100
	F-2				2	
	F-3				3	

with a scan rate of 5 mV s^{-1}, with the potential range from -0.764 to -0.164 V versus RHE prior to the test. All electrochemical measurements were performed at room temperature (25°C).

Data Availability

All data and materials used in this study are available from the corresponding author upon reasonable request.

References

1. I. A. Poimenidis et al., "Enhanced hydrogen production through alkaline electrolysis using laser-nanostructured nickel electrodes," *Int. J. Hydrogen Energy* **46**, 37162–37173 (2021).
2. A. M. Abdalla et al., "Hydrogen production, storage, transportation and key challenges with applications: a review," *Energy Convers. Manage.* **165**, 602–627 (2018).
3. M. Yu, K. Wang, and H. Vredenburg, "Insights into low-carbon hydrogen production methods: green, blue and aqua hydrogen," *Int. J. Hydrogen Energy* **46**, 21261–21273 (2021).
4. Z. Li et al., "Recent progress in low Pt content electrocatalysts for hydrogen evolution reaction," *Adv. Mater. Interfaces* **7**, 2000396 (2020).
5. W. Luo, Y. Wang, and C. Cheng, "Ru-based electrocatalysts for hydrogen evolution reaction: recent research advances and perspectives," *Mater. Today Phys.* **15**, 100274 (2020).
6. C. Li and J. B. Baek, "Recent advances in noble metal (Pt, Ru, and Ir)-based electrocatalysts for efficient hydrogen evolution reaction," *ACS Omega* **5**, 31–40 (2019).
7. X. Cui et al., "Monolithic nanoporous NiFe alloy by dealloying laser processed NiFeAl as electrocatalyst toward oxygen evolution reaction," *Int. J. Hydrogen Energy* **43**, 15234–15244 (2018).
8. J. Zhu et al., "Recent advances in electrocatalytic hydrogen evolution using nanoparticles," *Chem. Rev.* **120**, 851–918 (2019).
9. P. Bernard et al., "Demonstration of the influence of specific surface area on reaction rate in heterogeneous catalysis," *J. Chem. Educ.* **98**, 935–940 (2021).
10. E. Navarro Flores, Z. Chong, and S. Omanovic, "Characterization of Ni, NiMo, NiW and NiFe electroactive coatings as electrocatalysts for hydrogen evolution in an acidic medium," *J. Mol. Catal. A: Chem.* **226**, 179–197 (2005).
11. L. Lehmann et al., "Irregular electrodeposition of Cu-Sn alloy coatings in [EMIM] Cl outside the glove box with large layer thickness," *Coatings* **11**, 310 (2021).
12. B. Mahaling and D. S. Katti, "Fabrication of micro-structures of poly [(R)-3-hydroxybutyric acid] by electro-spraying/-spinning: understanding the influence of polymer concentration and solvent type," *J. Mater. Sci.* **49**, 4246–4260 (2014).
13. J. Salmones et al., "Textural characterisation of iron-promoted Raney nickel catalysts synthesised by mechanical alloying," *Adsorption Sci. Technol.* **19**, 871–885 (2001).
14. I. Brown and S. Sotiropoulos, "Preparation and characterization of microporous Ni coatings as hydrogen evolving cathodes," *J. Appl. Electrochem.* **30**, 107–111 (2000).
15. P. A. Nelson et al., "Mesoporous nickel/nickel oxide a nanoarchitectured electrode," *Chem. Mater.* **14**, 524–529 (2002).
16. Z. Lin and M. Hong, "Femtosecond laser precision engineering: from micron, submicron, to nanoscale," *Ultrafast Sci.* **2021**, 9783514 (2021).
17. D. Zhang et al., "Carbonized hybrid micro/nanostructured metasurfaces produced by femtosecond laser ablation in organic solvents for biomimetic antireflective surfaces," *ACS Appl. Nano Mater.* **3**, 1855–1871 (2020).
18. T. Y. Hwang, A. Vorobyev, and C. Guo, "Formation of solar absorber surface on nickel with femtosecond laser irradiation," *Appl. Phys. A* **108**, 299–303 (2012).
19. A. Abou Khalil et al., "Direct laser writing of a new type of waveguides in silver containing glasses," *Sci. Rep.* **7**, 11124 (2017).
20. D. J. Joe et al., "Laser–material interactions for flexible applications," *Adv. Mater.* **29**, 1606586 (2017).
21. S. Wang et al., "In situ synthesis of NiO at Ni micro/nanostructures as supercapacitor electrodes based on femtosecond laser adjusted electrochemical anodization," *Appl. Surf. Sci.* **541**, 148216 (2021).
22. A. Klos et al., "Ultrafast laser processing of nanostructured patterns for the control of cell adhesion and migration on titanium alloy," *Nanomaterials* **10**, 864 (2020).
23. Y. Huang et al., "Ultrafast hole deformation revealed by molecular attosecond interferometry," *Ultrafast Sci.* **2021**, 9837107 (2021).

24. B. Chandu et al., "Fabrication of nanocages on nickel using femtosecond laser ablation and trace level detection of malachite green and Nile blue dyes using surface enhanced Raman spectroscopic technique," *Opt. Laser Technol.* **131**, 106454 (2020).
25. B. K. Nayak and M. C. Gupta, "Self-organized micro/nano structures in metal surfaces by ultrafast laser irradiation," *Opt. Lasers Eng.* **48**, 940–949 (2010).
26. K. Sugioka and Y. Cheng, "Ultrafast lasers—reliable tools for advanced materials processing," *Light Sci. Appl.* **3**, e149 (2014).
27. S. A. Jalil et al., "Maskless formation of uniform subwavelength periodic surface structures by double temporally-delayed femtosecond laser beams," *Appl. Surf. Sci.* **471**, 516–520 (2019).
28. C. A. Zuhlke, T. P. Anderson, and D. R. Alexander, "Formation of multiscale surface structures on nickel via above surface growth and below surface growth mechanisms using femtosecond laser pulses," *Opt. Express* **21**, 8460–8473 (2013).
29. S. Kontermann et al., "Laser processed black silicon for photovoltaic applications," *Energy Procedia* **27**, 390–395 (2012).
30. G. Ou et al., "Large-scale hierarchical oxide nanostructures for high-performance electrocatalytic water splitting," *Nano Energy* **35**, 207–214 (2017).
31. Z. Li et al., "Significantly enhanced electrocatalytic activity of copper for hydrogen evolution reaction through femtosecond laser blackening," *Int. J. Hydrogen Energy* **46**, 10783–10788 (2021).
32. J. Yong et al., "Nature-inspired superwettability achieved by femtosecond lasers," *Ultrafast Sci.* **2022**, 9895418 (2022).
33. T. Baldacchini et al., "Superhydrophobic surfaces prepared by microstructuring of silicon using a femtosecond laser," *Langmuir* **22**, 4917–4919 (2006).
34. J. A. Cebollero et al., "Characterization of laser-processed thin ceramic membranes for electrolyte-supported solid oxide fuel cells," *Int. J. Hydrogen Energy* **42**, 13939–13948 (2017).
35. J. Wu et al., "Laser fabrication of bioinspired gradient surfaces for wettability applications," *Adv. Mater. Interfaces* **8**, 2001610 (2021).
36. A. Gabler et al., "Ultrashort pulse laser-structured nickel surfaces as hydrogen evolution electrodes for alkaline water electrolysis," *Int. J. Hydrogen Energy* **42**, 10826–10833 (2017).
37. T. Rauscher et al., "Femtosecond-laser structuring of Ni electrodes for highly active hydrogen evolution," *Electrochim. Acta* **247**, 1130–1139 (2017).
38. A. R. Neale et al., "Electrochemical performance of laser microstructured nickel oxyhydroxide cathodes," *J. Power Sources* **271**, 42–47 (2014).
39. C. Kerse et al., "Ablation-cooled material removal with ultrafast bursts of pulses," *Nature* **537**, 84–88 (2016).
40. L. Torrisi et al., "Nickel plasma produced by 532-nm and 1064-nm pulsed laser ablation," *Plasma Phys. Rep.* **34**, 547–554 (2008).
41. C. A. Zuhlke, T. P. Anderson, and D. R. Alexander, "Comparison of the structural and chemical composition of two unique micro/nanostructures produced by femtosecond laser interactions on nickel," *Appl. Phys. Lett.* **103**, 121603 (2013).
42. A. Nakhoul et al., "Self-organization regimes induced by ultrafast laser on surfaces in the tens of nanometer scales," *Nanomaterials* **11**, 1020 (2021).
43. K. Yin et al., "Micro torch assisted nanostructures' formation of nickel during femtosecond laser surface interactions," *Appl. Phys. Lett.* **108**, 241601 (2016).
44. Z. Li, X. Wei, and Z. Yang, "Pulsed laser 3D-micro/nanostructuring of materials for electrochemical energy storage and conversion," *Prog. Mater Sci.* **113**, 101052 (2022).
45. M. Gong et al., "Nanoscale nickel oxide/nickel heterostructures for active hydrogen evolution electrocatalysis," *Nat. Commun.* **5**, 4695 (2014).
46. M. Luo et al., "Insights into alloy/oxide or hydroxide interfaces in Ni–Mo-based electrocatalysts for hydrogen evolution under alkaline conditions," *Chem. Sci.* **14**, 3400–3414 (2023).
47. Z. Y. Zhang et al., "Cu-Zn-based alloy/oxide interfaces for enhanced electroreduction of CO_2 to C_{2+} products," *J. Energy Chem.* **83**, 90–97 (2023).
48. G. B. Darband, M. Aliofkhazraei, and A. S. Rouhaghdam, "Nickel nanocones as efficient and stable catalyst for electrochemical hydrogen evolution reaction," *Int. J. Hydrogen Energy* **42**, 14560–14565 (2017).
49. H. Herrera Hernandez et al., "Electrochemical impedance spectroscopy (EIS): a review study of basic aspects of the corrosion mechanism applied to steels," in *Electrochemical Impedance Spectroscopy*, M. El-Azazy, M. Min, and P. Annus, Eds., pp. 137–144, IntechOpen (2020).
50. W. Zhai et al., "Recent progress on the long-term stability of hydrogen evolution reaction electrocatalysts," *InfoMat* **4**, e12357 (2022).
51. S. Eliezer et al., "Synthesis of nanoparticles with femtosecond laser pulses," *Phys. Rev. B* **69**, 144119 (2004).

Biographies of the authors are not available.